Thermosolutal convection and solute segregation during the vertical Bridgman growth of Hg$_{1-x}$Cd$_x$Te single crystals

Lu Jun, Bai Bofeng *

State Key Laboratory of Multiphase Flow in Power Engineering, Xi'an Jiaotong University, No.28, Xianning West Road, Xi'an, Shaanxi 710049, People's Republic of China

ARTICLE INFO

ABSTRACT

The mechanism for thermosolutal convection and the coupling effects of flow, temperature and solute fields during the vertical Bridgman growth of Hg$_{1-x}$Cd$_x$Te single crystals have been numerically analyzed. The calculations take into account the thermophysical properties and their dependence on temperature and composition. The results show that there are two main thermal convection cells in the melt caused by two temperature gradients during the growth of Hg$_{1-x}$Cd$_x$Te single crystals. The stabilizing axial solute gradient in the melt will significantly damp the thermal convection cells when the absolute value of the solute Rayleigh number is close to the value of the thermal Rayleigh number. When there is a large solute gradient in the melt, the thermosolutal convection will become unstable, and the upper flow cell will evolve into a two-cell flow pattern. During the growth of Hg$_{1-x}$Cd$_x$Te single crystals, the radial solute segregation in the melt develops non-monotonically with two minima values. Thus, the methods that solely aim at either damping or enhancing the thermosolutal convection are not always able to improve the radial solute segregation.

© 2008 Elsevier B.V. All rights reserved.

1. Introduction

II–VI Semiconducting single crystals are widely used for devices operating in the infrared and near-infrared spectral regions [1,2]. These single crystals are often grown from the melt. Although the processing conditions for these single crystals differ from each other in some details, the quality of these crystals is governed by a similar set of mechanisms, which describe the processes of flow, heat and solute transport processes and the coupling effects between these processes. The corresponding important processing concepts and the key problems during the single-crystal growth from the melt were reviewed by Brown [3]. The vertical Bridgman configuration is one of the most popular techniques for the confined solidification growth of the II–VI semiconducting single crystals [4–6]. The three-zone furnace and the constant gradient furnace are the two main forms of the vertical Bridgman configurations in practice [7,8]. However, II–VI semiconducting single crystals grown by the vertical Bridgman

method often have defects associated with poor crystalline perfection and non-uniform composition distribution [9,10]. All the defects can be divided into two types: microscopic and macroscopic defects. The methods for improving the two types of defects are very different [11]. Due to the small typical scale of microscopic defects, these defects can be improved by heat treating after the growth processes. However, macroscopic defects have a large scale, which means that it is much more difficult to improve these defects after growth processes. In order to control the macroscopic defects in single crystals grown by the vertical Bridgman method, transport processes and coupling effects of flow, heat transfer and solute transfer during the growth of single crystals should be investigated in detail. In recent years, a lot of experimental and numerical research has been carried out. Wang experimentally measured the radial and axial solute segregations in single crystals grown in a three-zone furnace [12]. Adornato numerically studied the design effects of growth furnace and ampoule on the temperature field, the convection, the shape of melt–crystal interface and the solute macrosegregation in the crystal [13,14], and the author compared the numerical results with the experimental data from Wang [12]. The work was the first comparison between theoretical results and experimental

* Corresponding author. Tel.: +86 29 82665316; fax: +86 29 82669033.
E-mail address: bfbai@mail.xjtu.edu.cn (B. Bofeng).

data for single-crystal growth. Kim [15–17] numerically studied the importance of the damping effect of the solute gradient and the pulling rate of the ampoule during the single-crystal growth in the vertical Bridgman configuration by quasi-steady-state model and transient model, respectively. Dercy [18,19] studied the growth processes in the vertical Bridgman configuration by the $k–\varepsilon$ model. The research showed that laminar and turbulent models presented significant differences in the results of flow structure, concentration profiles, and the movement of melt–crystal interfaces. Based on the understanding of the physical mechanism of convection and the coupling effects of flow, heat transfer and solute transfer, the numerical parameter optimization method for the vertical Bridgman growth has been developed in recent years. Muller developed an overall design software to determine the detailed temperature profile in the growth furnace and provided useful information for optimization of the single-crystal growth [20]. This designed software was unable to analyze the solute profiles in the melt. Margulies obtained a small radial temperature gradient through optimizing the pulling rate and the temperature field in the growth furnace [21]. Capper developed a new method of accelerating crucible rotation technique (ACRT). By this method, a flatter solidification interface was obtained, and radial and axial solute segregations in single crystals were improved [22,23].

In the paper, numerical simulations of the growth of $Hg_{1−x}Cd_xTe$ single crystals in the vertical Bridgman configuration are carried out. The thermosolutal convection and the coupling effects of flow, heat transfer and solute transfer during the vertical Bridgman growth are studied in detail.

2. Formulation

2.1. Physical model

In the vertical Bridgman configuration, the cylindrical ampoule is placed at the axis of the growth furnace, and the melt is sealed in the cylindrical ampoule. The size and the shape of the crystal are determined by those of the ampoule. The three-zone furnace formed by the high isothermal, low isothermal and adiabatic zones is widely used for the single-crystal growth. The schematic diagram of the three-zone furnace is shown in Fig. 1.

The high and the low isothermal zones of the system are designed symmetrically. The medium value of the temperatures of two zones equals the solidifying point of $Hg_{1−x}Cd_xTe$ at $x = 0.2$. Neglecting the finite heat transfer between the furnace and ampoule, ideal heat transfer conditions are adopted from the following calculations.

2.2. Mathematical statement

Experimental data [24] showed that there were three stages during the single-crystal growth in the vertical Bridgman configuration, the initial transient stage, the middle steady stage and the final transient stage, as shown in Fig. 2.

During the period of the middle steady stage, the solidification rate of the crystal is equal to the pulling rate of the ampoule. Only during the period of the middle steady stage can the composition in the crystal reach the desired value. Thus, the pseudo-steady-state model (PSSM) is used to analyze the steady growth stage of $Hg_{1−x}Cd_xTe$ single crystals in the present work.

PSSM accounts for the translation of the ampoule by supplying the melt of a uniform composition C_0 to the top of the ampoule with a uniform velocity V_m, and at the same time, removing the crystal from the bottom of the ampoule with the pulling rate
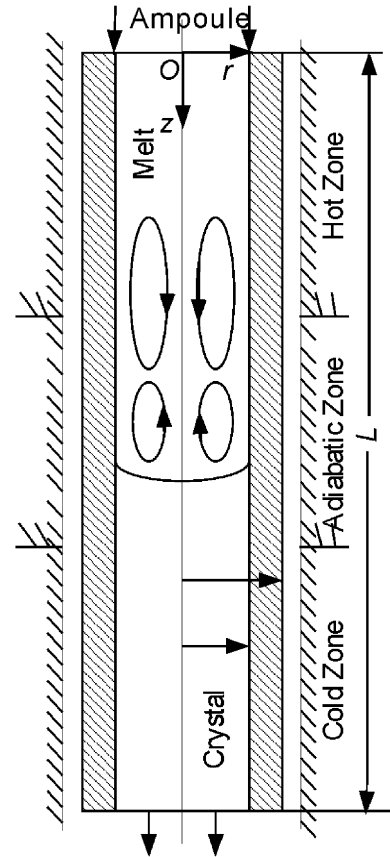

Fig. 1. Schematic diagram of the three-zone furnace.

$V_c=(\rho_c/\rho_m)V_m$, whose composition is the same as that of the melt. The above simplification neglects the initial and the final transient stages during single-crystal growth. Because of the very low velocity in the melt (μm/s in general), the flow pattern in the vertical Bridgman configuration is almost axisymmetric. The governing equations and the melt–crystal interface equation are written in a two-dimensional stationary cylindrical coordinate system, whose origin is at the top of the ampoule, as shown in Fig. 1. The spatial location of the melt–crystal interface is expressed as $h(r)$. The normal unit vector $\vec{n}$ and the tangential unit vector $\vec{t}$ of the melt–crystal interface are defined by

$$\vec{n} = \frac{\vec{e}_z − h_r\vec{e}_r}{(1 + h_r^2)^{1/2}}, \quad \vec{t} = \frac{\vec{e}_r + h_r\vec{e}_z}{(1 + h_r^2)^{1/2}} \tag{1}$$

where $h_r=\partial h/\partial r$ and $\vec{e}_z, \vec{e}_r$ are the unit vectors of the axial and the radial coordinates, respectively.

Because the flow pattern in the melt is almost axisymmetric, calculations are carried out only in the right section of the ampoule in this work. The mathematical equations consist of: the energy balance equations in the melt, crystal and ampoule; the momentum equation, the species conservation equation and the continuity equation in the melt; and the location equation of the melt–crystal interface. All equations are expressed in dimensionless form by scaling lengths with the ampoule height L, velocities with α_m/L and pressure with $\rho_m\alpha_m^2/L^2$. Meanwhile, the dimensionless concentration and temperature differences are defined as $S(r,z) = C/C_0−1$ and $\theta(r,z)=(T−T_L)/(T_H−T_L)$, respectively.

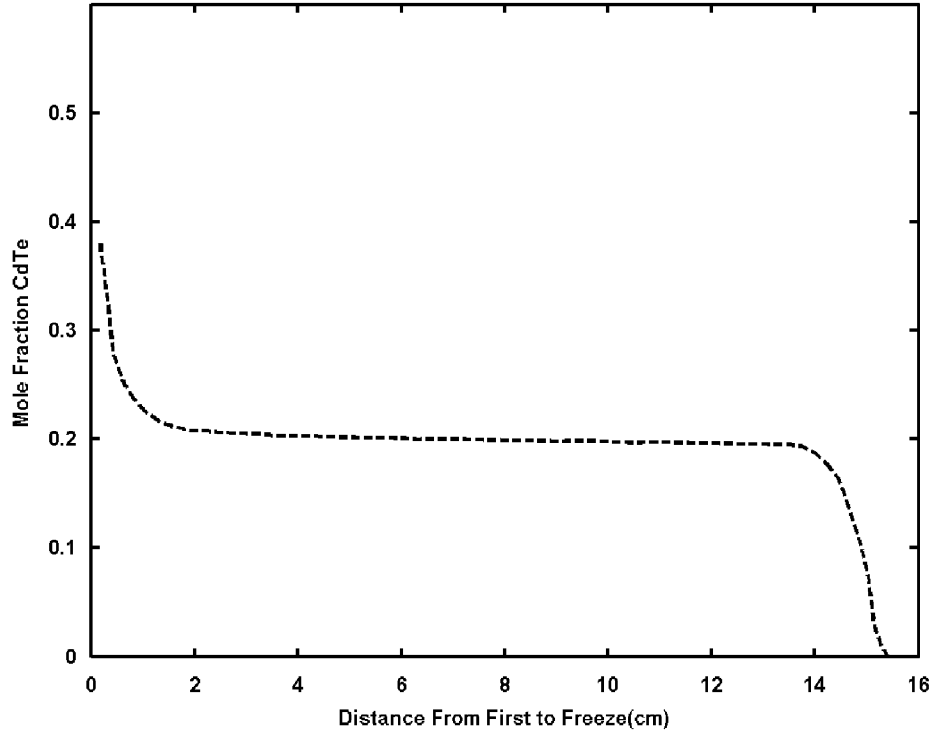The dimensionless governing equations are

$$\nabla \cdot \vec{V} = 0 \tag{2}$$

Fig. 2. CdTe composition versus axial position for the $Hg_{1-x}Cd_xTe$ ($x=0.2$) single crystal.

$$\vec{V} \cdot \nabla U = -\frac{\partial p}{\partial z} + Pr\nabla^2 U + Pr(Ra_s S - Ra_t(\theta - 1)) \tag{3}$$

$$\vec{V} \cdot \nabla V = -\frac{\partial p}{\partial r} + Pr\nabla^2 V \tag{4}$$

$$\vec{V} \cdot \nabla \theta = \nabla^2 \theta \tag{5}$$

$$\vec{V} \cdot \nabla S = \frac{Pr}{Sc}\nabla^2 S \tag{6}$$

$$Pe\vec{e}_z \cdot \nabla \theta = \chi_c \nabla^2 \theta \tag{7}$$

$$Pe\vec{e}_z \cdot \nabla \theta = \chi_a \nabla^2 \theta \tag{8}$$

Assuming the liquidus line of the $Hg_{1-x}Cd_xTe$ alloy is a straight line and taking the solidifying point at the concentration C_0/κ as the reference temperature θ_m^0, the dimensionless melt–crystal interface equation is written as

$$\theta(r, h(r)) = \theta_m^0 + m(S + 1 - 1/\kappa) \tag{9}$$

Because densities of the melt and crystal are almost equal, the dimensionless velocity boundary conditions can be written as

$z = 0 : U = Pe, \quad V = 0$
$z = 1 : U = Pe, \quad V = 0$
$r = 0 : \partial U/\partial r = 0, \quad V = 0$
$r = \Lambda : U = Pe, \quad V = 0 \tag{10}$

where Λ is the dimensionless outer radius of the ampoule.

The dimensionless solute boundary conditions are

$z = 0 : S = 0$
$z = 1 : S = 0$
$r = 0 : \partial S/\partial r = 0$
$r = \Lambda : \partial S/\partial r = 0 \tag{11}$

The dimensionless temperature boundary conditions are

$z = 0 : \theta = 1.0$
$z = 1 : \theta = 0$
$r = 0 : \partial \theta/\partial r = 0$
$$r = \Lambda : \begin{cases} \theta = 1.0, & \text{high zone} \\ \theta = 0, & \text{low zone} \\ \partial\theta/\partial r = 0, & \text{adiabatic zone} \end{cases} \tag{12}$$

The dimensionless boundary conditions at the melt–ampoule interface are

$$U_m|_{r=\delta_m} = Pe \quad V_m|_{r=\delta_m} = 0$$
$$\left.\frac{\partial\theta}{\partial r}\right|_{r=\delta_m} = K_a\left.\frac{\partial\theta}{\partial r}\right|_{r=\delta_a} \quad \left.\frac{\partial S}{\partial r}\right|_{r=\delta_m} = 0 \tag{13}$$

The dimensionless boundary condition at crystal–ampoule interface is

$$K_c\left.\frac{\partial\theta}{\partial r}\right|_{r=\delta_c} = K_a\left.\frac{\partial\theta}{\partial r}\right|_{r=\delta_a} \tag{14}$$

The dimensionless boundary conditions at the melt–crystal interface are

$$\vec{V} \cdot \vec{t} = Pe(\vec{e}_z \cdot \vec{t}), \quad \vec{V} \cdot \vec{n} = Pe(\vec{e}_z \cdot \vec{n}) \tag{15}$$

$$(\vec{n} \cdot \nabla\theta)_m - K_c(\vec{n} \cdot \nabla\theta) = StPe(\vec{n} \cdot \vec{e}_z) \tag{16}$$

$$(\vec{n} \cdot \nabla S)_m = \frac{PeSc}{Pr}(1 - \kappa)(S + 1)(\vec{e}_z \cdot \vec{n}) \tag{17}$$

The subscripts m, c and a donate the melt, the crystal and the ampoule, respectively. The dimensionless groups in the above equations are defined in Table 1.

2.3. Numerical scheme

A nonuniform grid of 200×20 was used in the calculations of the single-crystal growth in the three-zone furnace, as shown in Fig. 3. The meshes in the melt zone are gradually refined from the centre of the melt zone to the top of the ampoule, the melt–crystal interface, the axial line of the ampoule, and the melt–ampoule interface. The meshes in other calculation zones are uniform. The mesh density in the melt zone is twice as high as that in the crystal and ampoule zones. It has been shown that the calculation results based on this grid are grid-independent solutions.

The pressure–velocity coupling is solved by the SIMPLER algorithm. The shape of the melt–crystal interface is described by the staircase approaching method and solved iteratively. The convection terms are discretized by the power-law scheme, and diffusion terms are discretized by the central difference scheme. The discretized equations are solved by the alternate direction iteration method.

Calculations start with the melt–crystal interface determined by the initial temperature profile. Under the fixed melt–crystal interface conditions, the convergence criterion is satisfied when the absolute values of the maximum relative variation of all calculated variables between successive iterations are $< 10^{-6}$. Then, a new melt–crystal interface is obtained by formula (9), and the comparison of the previous and new melt–crystal interfaces is performed. If there is any difference between the positions of the two interfaces, the calculation will be carried out repeatedly. Otherwise the calculations stop.

2.4. Thermophysical properties

In order to obtain more accurate calculated results, the thermophysical properties and their dependence on temperature and composition should be used. All the data [25–30] are expressed as a function of temperature and composition in this paper.

Liquidus line

$$T_m(x) = 670 + 422 \times (a_1 x + a_2 x^{3/2} + a_3 x^{5/2}) \tag{18}$$

where T_m is in °C. The coefficients $\{a_i\}$ in formula (18) are {1.9967, -1.3101, 0.3146}. x is the mole fraction of CdTe and $x \in [0,1]$.

Table 1
The dimensionless groups.

Quantity	Definition
Prandtl number	$Pr = \gamma_m / \alpha_m$
Schmidt number	$Sc = \gamma_m / D_m$
Thermal Rayleigh number	$Ra_t = (\beta_T L^3 g(T_H - T_L)) / \gamma_m \alpha_m)$
Solute Rayleigh number	$Ra_s = (\beta_s L^3 g C_0) / (\gamma_m \alpha_m)$
Ratio of thermal conductivities	$K = \lambda / \lambda_m$
Ratio of thermal diffusivities	$\chi = \alpha / \alpha_m$
Stephan number	$St = \Delta h_f / (c_{pm}(T_H - T_L))$
Peclet number	$Pe = V_g / (\alpha_m / L)$

Solidus line

$$
\begin{aligned}
T_c(x) = 670 + 422 \times [&b_1(2x^2 - 1) + b_2 \cos x \\
&+ b_3 e^{2x^2 - 1} + b_4 \ln(1 + x) + b_5(e^x - 1)]
\end{aligned} \tag{19}
$$

where T_c is in °C. The coefficients $\{b_i\}$ are {7.5101, 7.3069, 0.5564, 12.3343, -11.9492}. x is the mole fraction of CdTe and $x \in [0,1]$.

Specific heat of the melt

$$
\begin{aligned}
c_{pm}(x, T) = (c_1 x + c_2 x^2 + c_3 x^3) + (c_4 + c_5 x \\
+ c_6 x^2 + c_7 x^3) \frac{T}{10^3} + (c_8 + c_9 x) \left(\frac{10^3}{T}\right)^2
\end{aligned} \tag{20}
$$

where c_{pm} is in cal/g · °C. The coefficients $\{c_i\}$ are {-0.1603, 0.4637, -0.6013, 0.03426, 0.0661, -0.2970, 0.4503, 0.01056, 0.1023}. T is the temperature of the melt expressed in °C. x is the mole fraction of CdTe and $x \in [0,1]$.

Specific heat of the crystal

$$c_{pc}(x, T) = \left[(12.45 - 2.88x + (2.17 + 5.73x)\frac{T}{10^3}\right]/M(x) \tag{21}$$

where c_{pc} is in cal/g °C. T is the temperature of the crystal expressed in °C. x is the mole fraction of CdTe and $x \in [0,1]$. $M(x)$ is the mole mass of $Hg_{1-x}Cd_x Te$ expressed in g/mol.

Density of the melt

$$\rho_m(x, T) = d_1 + d_2 x + (d_3 + d_4 x)\frac{T}{10^3} \tag{22}$$

where ρ_m is in g/cm^3. The coefficients $\{d_i\}$ are {7.8971, -0.7263, 0.1885, -2.2213}. T is the temperature of the melt and $T \in [680,835]$ °C. x is the mole fraction of CdTe and $x \in [0,0.2]$.

Density of the crystal

$$\rho_c(x) = 8.077 - 2.225x \tag{23}$$

where ρ_c is in g/cm^3. x is the mole fraction of CdTe and $x \in [0,1]$.

It is difficult to measure the thermal conductivities, but we can calculate the thermal conductivities of $Hg_{1-x}Cd_x Te$ by the formula $\lambda = \rho c_P \alpha$.

Thermal diffusivity of the melt

$$\alpha_m(x, T) = B \ln T - A \tag{24}$$

where α_m is in mm^2/s. T is in °C and $T \in [670,841]$ °C. x is the mole fraction of CdTe and $x \in [0,0.301]$. B and A are coefficients depending on the mole fraction of CdTe.

Thermal diffusivity of the crystal

$$\alpha_c(x, T) = A_0 - A_1 T + A_2 T^2 - A_3 T^3 \tag{25}$$

where α_c is in mm^2/s. T is in °C/1000 and $T \in [670,727]$ °C. x is the mole fraction of CdTe and $x \in [0,0.301]$. A_0, A_1, A_2 and A_3 are coefficients depending on the mole fraction of CdTe.

Here, the coefficients of the above two formulas are expressed in quartic function of composition as $\sum_{i=1}^{5} c_i x^{5-i}$. $\{c_i\}$ are shown in Table 2.
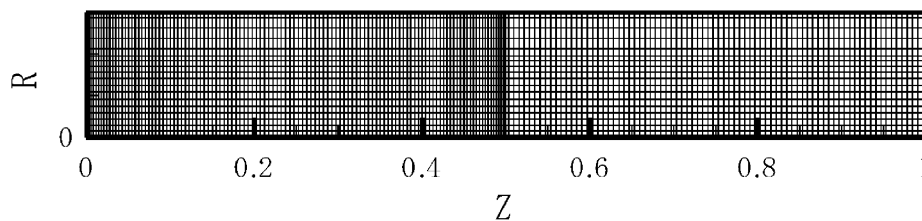

Fig. 3. Calculation grid used in three-zone furnace.

Table 2
The coefficients of the functions of B, A and A_i.

	c_1	c_2	c_3	c_4	c_5
B	9585	−6295	1362	−116.90	10.47
A	62,781	−41,191	8893	−756.73	67.40
A_0	2772	−1777	384	−36.04	2.78
A_1	19,175	−11,606	2236	−162.08	9.94
A_2	49,858	−30,112	5728	−386.93	20.98
A_3	42,900	−26,017	5016	−338.88	16.21

Table 3
The thermophysical properties of the ampoule and the geometric parameters of the vertical Bridgman configuration.

Quantity	Symbol (units)	Value
Thermal conductivity	λ_a (W/K cm)	0.025
Density	ρ_a (g/cm^3)	2.2
Specific heat	c_{pa} (J/Kg)	1.05
Ampoule length	L (cm)	6
Length of gradient zone	L_A (cm)	1.5
Crystal radius	R_c (cm)	0.6
Outer radius of ampoule	R_a (cm)	0.9
Solidifying point at $x=0.2$	T_0 (°C)	702
Temperature difference	T_H-T_L (°C)	300
Initial mole fraction of CdTe	C_0	0.2
Pulling rate	V_g (µm/s)	0.2

Mass diffusivity of CdTe in the crystal

$$D_c(x,T) = 3.15 \times 10^{10} \times 10^{-3.53x} \exp\left(-\frac{2.24 \times 10^4}{T}\right) \tag{26}$$

where D_c is in µm^2/s. T is in K and $T \in [673,973] K$. x is the mole fraction of CdTe and $x \in [0,0.3]$.

Equilibrium segregation coefficient

$$\kappa = (0.210 + 0.790x)^{-1} \tag{27}$$

where x is the mole fraction of CdTe and $x \in [0,1]$.

There are not many experimental data of other thermophysical properties used in the calculations, so the values at $x=0.2$ are used instead [16].

Mass diffusivity of CdTe in the melt

$$D_l = 5.5 \times 10^{-5} \text{ cm}^2/\text{s}$$

Kinetic viscosity of the melt

$$v = 1.08 \times 10^{-3} \text{ cm}^2/\text{s}$$

Thermal expansion coefficient in the melt

$$\beta_T = 7.95 \times 10^{-5} \text{ 1/°C}$$

Solutal expansion coefficient in the melt

$$\beta_c = -0.305 \text{ 1/mol (CdTe)}$$

Latent heat of solidification

$$\Delta h_f = 130.4 \text{ J/g}$$

In all the calculations, the units of all the above thermophysical properties were converted into international units. The fitting errors of all the above formulas are <2.5%.

The thermophysical properties of the ampoule and the geometric parameters of the vertical Bridgman configuration used in the calculations are listed in Table 3.

It seems that either the upper limit or the lower limit of temperature in Table 3 is out of the temperature ranges in formulas (22), (24)–(26), so we have to extrapolate these formulas to the corresponding temperature ranges to calculate those thermophysical properties.

3. Results and discussions

As shown in formulas (2)–(8), the most important dimensionless non-thermophysical parameters in the governing equations are the thermal Rayleigh number, the solutal Rayleigh number and the Peclet number. In this paper, the thermosolutal convection and the coupling effects of flow, heat and solute transfer processes during the growth of Hg$_{1-x}$Cd$_x$Te single crystals are exemplified by the calculations under two conditions: one is increasing the thermal Rayleigh number from $Ra_t=0$ to $Ra_t=1.0 \times 10^9$ at the fixed solute Rayleigh number $Ra_s=0$, and the other is decreasing the solute Rayleigh number from $Ra_s=0$ to $Ra_s=-1.0 \times 10^9$ at the fixed thermal Rayleigh number $Ra_t=1.0 \times 10^9$. The main calculation results of the temperature, flow and solute concentration fields are shown below.

3.1. Temperature profiles

The temperature profiles under different conditions are shown in Fig. 4. As shown in Fig. 4, the temperature profiles under all the conditions are similar to each other. The reason for this is that the Prandtl number of the Hg$_{1-x}$Cd$_x$Te melt is small, which makes the temperature profiles hardly affected by the flow in the melt. When the thermal Rayleigh number is very large, the isothermal lines in the melt will become flat and will be almost parallel to each other. At this time, there is a well-mixed zone of temperature in the melt. The isothermal lines in the crystal are still almost the same as those under other conditions.

The radial temperature gradient is defined as the biggest temperature difference of the axial cross-sections

$$GT_{radial} = (T(n,m)) - (T(n,:1)) \tag{28}$$

where n is the serial number of calculation nodes in z-direction and $n=1,\ldots,200$. m is the serial number of nodes at the inner wall of the ampoule in r-direction.

The radial temperature gradients under different conditions are shown in Fig. 5. In Fig. 5, the negative values reflect the cross-temperature field with higher temperature at the centerline of the ampoule, while lower temperature is at the wall of the ampoule, and vice versa.

As shown in Fig. 5, there are two peaks of the radial temperature gradients along the axial position of the ampoule. The axial positions of the two peaks are at the intersection of the high isothermal zone and the adiabatic zone, and at the intersection of the low isothermal zone and the adiabatic zone, respectively. The radial temperature gradients in the crystal are almost similar to each other, while the radial temperature gradients in the melt are very different. When $Ra_t=0,Ra_s=0$, the radial temperature gradients in the melt are the largest, which gradually decrease as the thermal Rayleigh number increases. The reason for this is that the flow intensity in the melt will increase as the thermal Rayleigh number increases, making the radial temperature gradients smaller due to the mixing effect. When $Ra_t=10^9$, the radial temperature gradient in the melt has almost disappeared. Gradually reducing the solute Rayleigh number at fixed thermal Rayleigh number $Ra_t=10^9$, the flow intensity in the melt will decrease because of the damping effect of the axial solute gradient. Under these conditions the mixing effect of flow will become weak, and the radial temperature gradients will increase reversely.
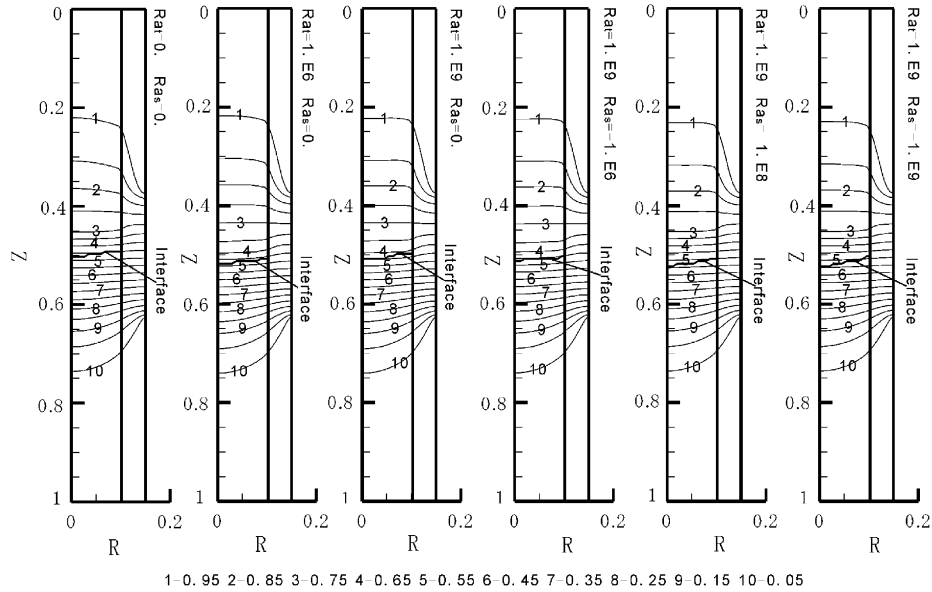
1–0.95 2–0.85 3–0.75 4–0.65 5–0.55 6–0.45 7–0.35 8–0.25 9–0.15 10–0.05

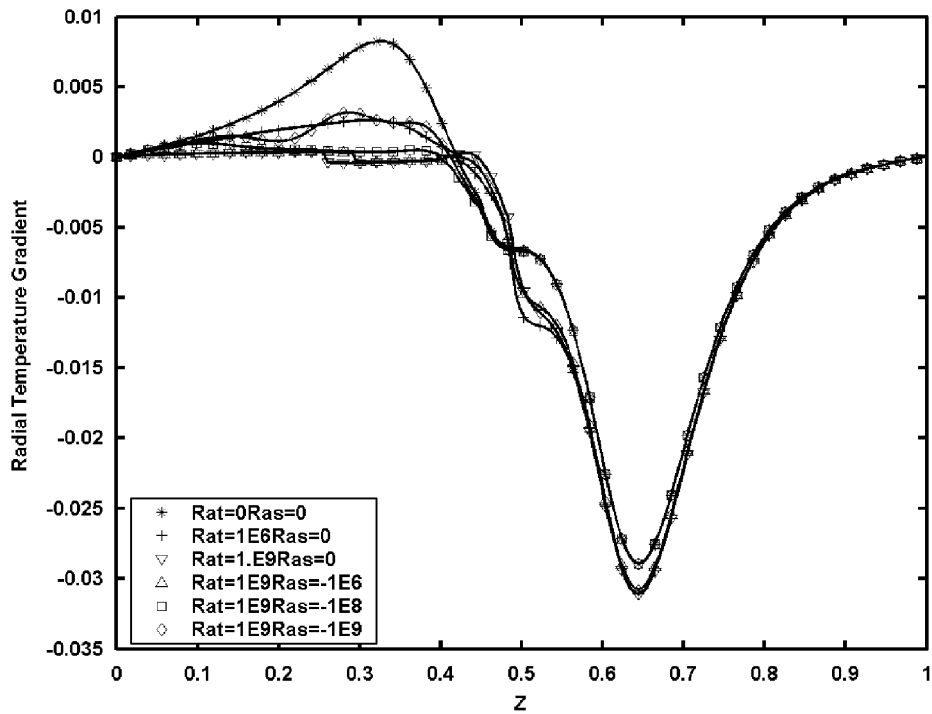Fig. 4. Temperature profiles calculated in the ampoule.

Fig. 5. The radial temperature gradients along the axial position of the ampoule.

3.2. Flow fields

The stream function profiles calculated under different conditions are presented in Fig. 6. The flow directions with negative values of stream function are considered as clockwise, and vice versa.

As shown in Fig. 6, there are two main flow cells in the melt except at $Ra_t=Ra_s=0$. At this time, there is only the force flow caused by the pull of the ampoule. As the thermal Rayleigh number increases at $Ra_s=0$, there exist thermal convection cells in the melt, and the intensity of those cells will increase as the increase of the thermal Rayleigh number. As the thermal Rayleigh number increases, the intensity of the lower cells approaches that of the upper cells. Because the decrease in the solute Rayleigh number means the increase in stabilizing solute gradients in the melt, the flow intensity will decrease with reduction in the solute Rayleigh number at $Ra_t=10^9$. The damping effect of the stabilizing solute gradients on the lower flow cells is more significant than on the upper flow cells. When the solute Rayleigh number decreases from 0 to -10^6, the intensity of the flow cells will not decrease significantly. Only when the absolute value of the solute Rayleigh number is close to the value of the thermal Rayleigh number will the damping effect of the solute gradients be significant. If the solute Rayleigh number approaches -10^9, secondary weak flow cells will appear near the upper flow cell, and the upper flow cell will evolve into a two-cell flow construction.
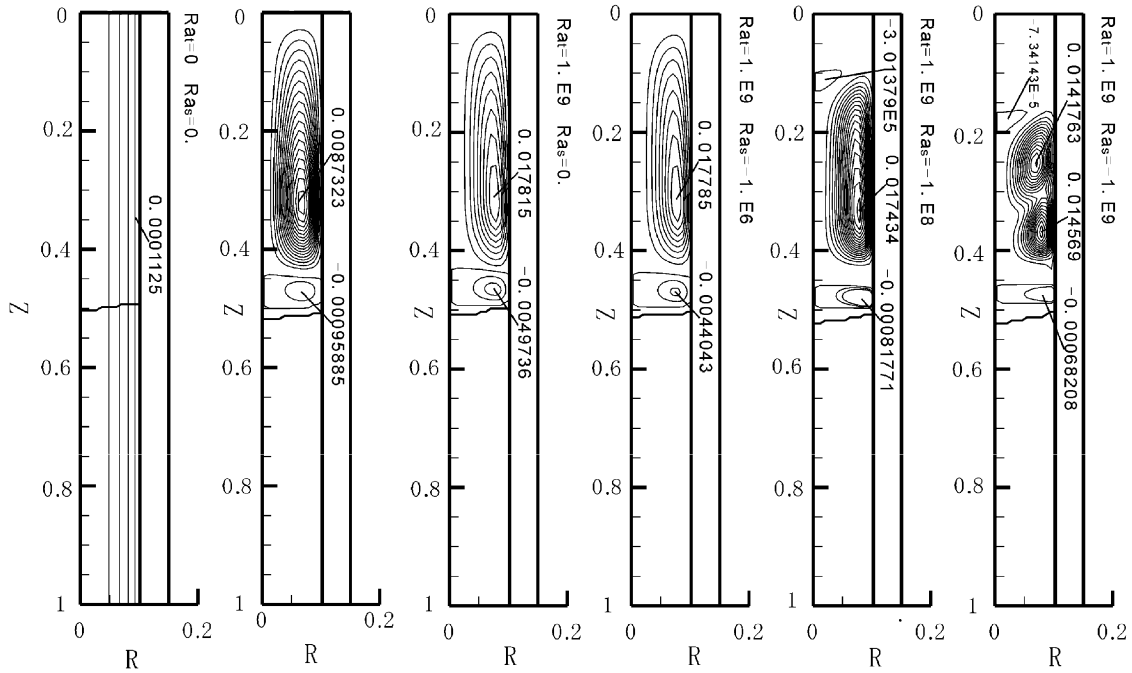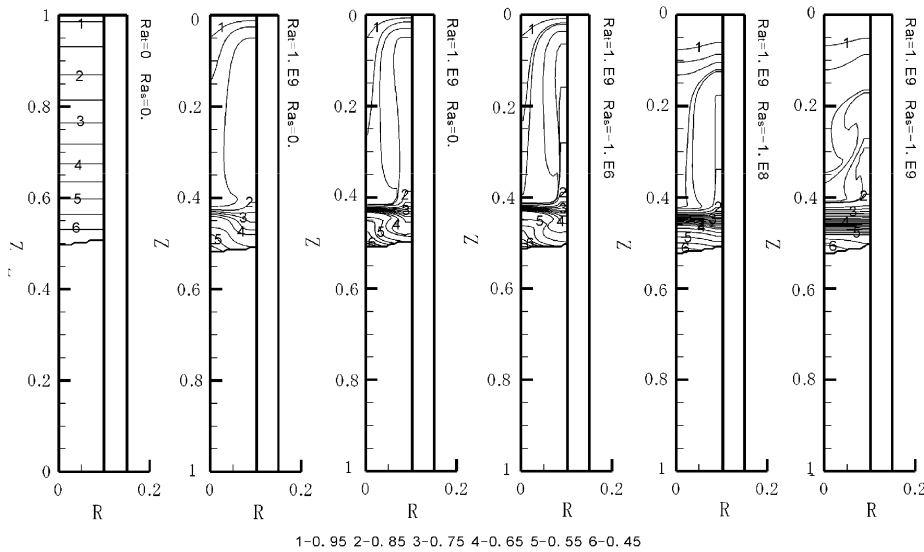
Fig. 6. Flow-field profiles calculated in the ampoule.

1-0.95 2-0.85 3-0.75 4-0.65 5-0.55 6-0.45

Fig. 7. Solute profiles calculated in the ampoule.

3.3. Solute profiles

The solute profiles corresponding to the flow fields in Fig. 6 are shown in Fig. 7. The values shown in Fig. 7 are c/c_0.

Because the equilibrium segregation coefficient of $Hg_{1-x}Cd_xTe$ alloy is larger than unity, the CdTe solute will enter the crystal preferentially and an abundant HgTe area will form near the interface during the solidification processes. Furthermore, because HgTe composition is heavier than CdTe, the axial solute gradient in the melt is stabilizing. As shown in Fig. 7, when there is no natural convection in the melt at $Ra_t=Ra_s=0$, the solute profile is almost an exponential pattern and isoconcentration lines in the melt are horizontal and parallel to each other. As the thermal Rayleigh number increases, natural convection cells will appear in

the melt, and due to the large Schmidt number of the $Hg_{1-x}Cd_xTe$ alloy, the effects of the natural convection cells on the solute profiles are significant. When there are two main convection cells in the melt, two well-mixed solute zones will appear. As shown in Fig. 6, the directions of lower flow cells are clockwise, so the abundant HgTe composition in this area is carried to the centerline of ampoule. Thus, the solute profiles at a given axial location in the lower melt decreases from the wall to the centerline of the ampoule, while that in the upper melt is reverse. When the upper flow cells become unstable and evolve into a two-cell flow construction, three well-mixed solute zones will appear in the melt. When the decrease of the solute Rayleigh number is enough to damp the convection obviously, the distorted isoconcentration lines will become flatter.
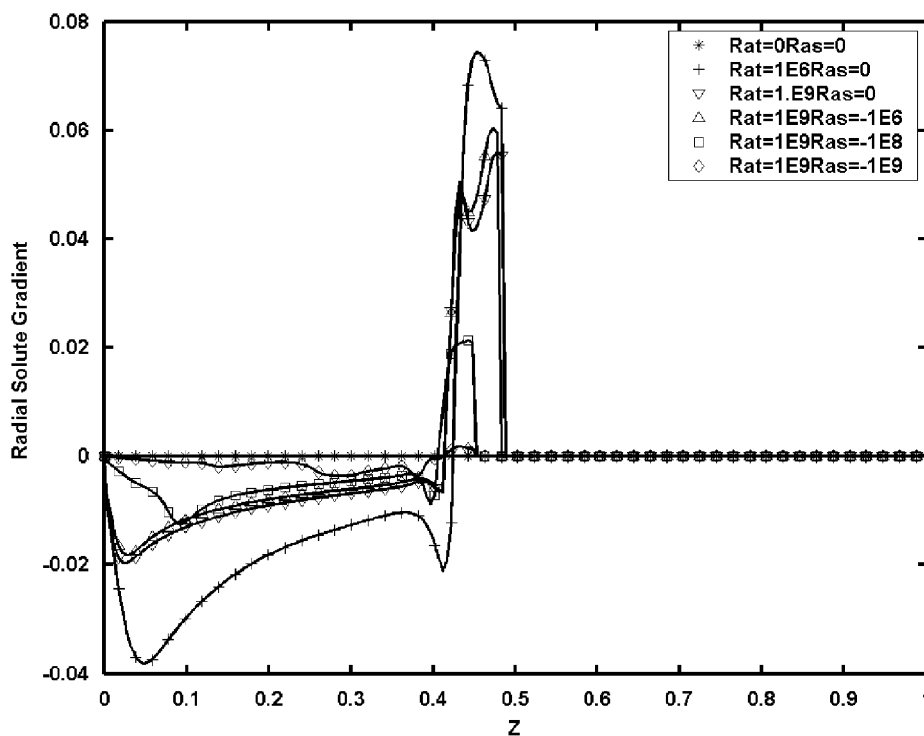
Fig. 8. The radial solute gradients along the axial positions of the ampoule.

The radial solute gradient is defined as the biggest solute concentration difference of the axial cross-sections

$$GS_{radial} = S(n, m) - S(n, 1) \tag{29}$$

where n is the serial number of calculation nodes in z-direction and $n=1,\ldots,200$. m is the serial number of nodes at the inner wall of the ampoule in r-direction.

The radial solute gradients are shown in Fig. 8. In Fig. 8, the negative values reflect the cross-solute profile with higher concentration at axial line, while lower concentration is at wall, and vice versa.

As shown in Fig. 8, when $Ra_t=Ra_s=0$, the radial solute segregation in the melt is almost zero. Because the solute segregation in the crystal is determined by the radial solute segregation in the lower melt, just the radial solute segregation in the lower melt is discussed here. When the thermal Rayleigh number increases at the fixed solute Rayleigh number $Ra_s = 0$, the intensity of flow and the radial solute segregation both increase. However, when $Ra_t > 10^6$ the radial solute segregation decreases as the thermal Rayleigh number increases. At this time, there are two well-mixed solute areas in the melt, and a smaller radial solute segregation is obtained. When reducing the solute Rayleigh number at $Ra_t = 10^9$, the intensity of flow will decrease and the mixing effect in the melt will become weaker. So the radial solute segregation will be worse again. When the damping effect of the axial solute gradients is significant, the intensity of flow will decrease obviously, and the radial solute segregation will be improved again. From Fig. 8, we see that the radial solute segregation in the melt undergoes a non-monotonic evolution during the growth.

4. Conclusions

The numerical calculations of the single-crystal growth of $Hg_{1-x}Cd_xTe$ in the vertical Bridgman configuration have been carried out. The main results are as follows:

(1) The stabilizing solute gradients will damp the convection caused by temperature gradients in the melt. Only when the absolute value of the solute Rayleigh number is close to the value of the thermal Rayleigh number will the damping effects of the solute gradients be significant.
(2) When the solute gradient is large, the upper flow in the melt will become unstable and will evolve into a two-cell construction.
(3) The radial solute segregation undergoes a non-monotonic evolution during growth processes. Thus, the methods that just aim at damping or enhancing the thermosolutal convection are not always able to improve the radial solute segregation. Damping or enhancing the convection after judging the range of the flow intensity during a real growth process is a more feasible method.

Acknowledgments

References

[1] W.D. Lawson, S. Nielsen, E.H. Putley, A.S. Young, J. Phys. Chem. Solids 9 (1959) 309.
[2] D. Long, J.L. Schmit, Mercury–Cadmium Telluride and Closely Related Alloys, Semiconductors and Semimetals, Academic Press, New York, 1970 p. 175.
[3] R.A. Brown, AICHE J. 6 (1986) 881.
[4] E.M. Monberg, W.A. Gault, F. Simchock, F. Domingguez, J. Crystal Growth 83 (1987) 174.
[5] K. Hoshikawa, H. Nakanishi, H. Kohda, M. Sasaura, J. Crystal Growth 94 (1989) 643.
[6] P. Rudolph, Prog. Cryst. Growth Charact. Mater. 29 (1994) 275.
[7] C.A. Wang, A.F. Witt, J.R. Carruthers, J. Crystal Growth 66 (1984) 299.

[8] A. Rouzaud, D. Camel, J.J. Favier, J. Crystal Growth 73 (1985) 149.

[9] B.E. Bartlett, P. Capper, J.E. Harris, M.J.T. Quelch, J. Crystal Growth 46 (1979) 623.

[10] P. Rudolph, M. Muhlberg, Mater. Sci. Eng. B 16 (1993) 8.

[11] G. Muller, Convection and Inhomogeneities in Crystal Growth from the Melt. Crystal: Growth, Properties, and Applications, Vol. 12, Springer, Berlin, 1988.

[12] C.A. Wang. Ph.D. Thesis, Mass. Inst. Technol. Cambridge.

[13] P.M. Adornato, R.A. Brown, J. Crystal Growth 7 (1987) 155.

[14] P.M. Adornato, R.A. Brown, Int. J. Numer. Methods, FL 7 (1987) 761.

[15] D.H. Kim, P.M. Adornato, R.A. Brown, J. Crystal Growth 89 (1988) 339.

[16] D.H. Kim, R.A. Brown, J. Crystal Growth 96 (1989) 609.

[17] D.H. Kim, R.A. Brown, J. Crystal Growth 114 (1991) 411.

[18] R. Cerny, A. Kalbac, P. Prikryl, Comput. Mater. Sci. 17 (2000) 34.

[19] R. Cerny, P. Jelinek, P. Prikryl, Comput. Mater. Sci. 25 (2000) 316.

[20] G. Muller, J. Friedrich, J. Crystal Growth 266 (2004) 1.

[21] M. Margulies, P. Witomski, T. Duffar, J. Crystal Growth 266 (2004) 175.

[22] P. Capper, Prog. Cryst. Growth CH 28 (1994) 165.

[23] P. Capper, C. Maxey, C. Bulter, M. Grist, J. Price, J. Crystal Growth 275 (2005) 259.

[24] F.R. Szofran, D. Chandra, J.-C. Wang, E.K. Cothran, S.L. Lehoczky, J. Crystal Growth. 70 (1984) 343.

[25] L.R. Holland, R.E. Taylor, J. Vac. Sci. Technol. A 1 (1983) 1615.

[26] D. Chandra, L.R. Holland, J. Vac. Sci. Technol. A 1 (1983) 1620.

[27] J.C. Brice, P. Capper, J. Crystal Growth 75 (1986) 395.

[28] C.H. Su, J. Crystal Growth 78 (1986) 51.

[29] K. Zanio, Tom Massopust, J. Electron. Mater. 15 (1986) 103.

[30] V. Alexiades. ORNL/TM-11734, 1991.